



HAL
open science

Tin stable isotopes in magmatic-affected coal deposits: Insights in the geochemical behavior of tin

Qinyuan Qu, Guijian Liu, Manuel Henry, David Point, Jérôme Chmeleff,
Ruoyu Sun, Jeroen E. Sonke, Jiubin Chen

► To cite this version:

Qinyuan Qu, Guijian Liu, Manuel Henry, David Point, Jérôme Chmeleff, et al.. Tin stable isotopes in magmatic-affected coal deposits: Insights in the geochemical behavior of tin. *Applied Geochemistry*, 2020, 119, pp.104641 -. 10.1016/j.apgeochem.2020.104641 . hal-03490798

HAL Id: hal-03490798

<https://hal.science/hal-03490798v1>

Submitted on 6 Jun 2022

HAL is a multi-disciplinary open access archive for the deposit and dissemination of scientific research documents, whether they are published or not. The documents may come from teaching and research institutions in France or abroad, or from public or private research centers.

L'archive ouverte pluridisciplinaire **HAL**, est destinée au dépôt et à la diffusion de documents scientifiques de niveau recherche, publiés ou non, émanant des établissements d'enseignement et de recherche français ou étrangers, des laboratoires publics ou privés.



Distributed under a Creative Commons Attribution - NonCommercial 4.0 International License

1 Tin stable isotopes in magmatic-affected coal 2 deposits: Insights in the geochemical behavior 3 of tin

4 Qinyuan Qu^{1,2,3}, Guijian Liu², Emmanuel Henry³, David Point³, Jérôme Chmeleff³, Ruoyu Sun¹,
5 Jeroen E. Sonke^{3*}, Jinbin Chen^{1*}

6
7 ¹ Institute of Surface Earth System Science, Tianjin University, Tianjin, China

8 ² CAS Key Laboratory of Crust-Mantle Materials and Environment, School of Earth and Space
9 Sciences, University of Science and Technology of China, Hefei, Anhui 230026, China;

10 ³ Géosciences Environnement Toulouse, Observatoire Midi-Pyrénées, CNRS/IRD/Université Paul
11 Sabatier Toulouse III, France

12

13 Corresponding author:

14 jeroen.sonke@get.omp.eu

15 jbchen@tju.edu.cn

16

17 **Abstract:**

18 Tin (Sn) is a redox-sensitive element and geochemically incompatible that accumulates in
19 evolved magmas and associated hydrothermal fluids. Here, a Sn stable isotope approach is used to
20 characterize sources and geochemical behaviors of Sn in magmatic intruded coal deposits by
21 combining with petrographic and elemental analysis. Sn isotope ratios of twelve coal samples with
22 various magmatic-affected degrees show a $\delta^{120/118}\text{Sn}$ variation from -0.06 to 0.22‰ (2σ of 0.07‰,
23 relative to NIST 3161a). Basing on Sn isotope data and geochemical characteristics of the samples,
24 we suggest binary source mixing and redox state related isotope shift as two mechanisms
25 accounting for the isotope variations. The first mechanism is an admixture of
26 magmatic-hydrothermal fluids, characterized by high $\delta^{120/118}\text{Sn}$, into coal deposits with low
27 $\delta^{120/118}\text{Sn}$. A binary mixing model is used to estimate Sn contributions of the two end-members.
28 The second process results in a positive isotope shift caused by an oxidation of sample states when
29 they are affected by magmatic intrusions. In fact, magmatic intrusions could trigger the oxidation

1

30 of Sn, resulting in heavy Sn isotope enrichment in the magmatic affected samples. The change in
31 coal redox-state is supported by a concomitant change of redox proxies, such as V/(V+Ni), Mn/Cr
32 and V/Cr. The enrichment of heavy Sn isotopes in samples impacted by magmatic hydrothermal
33 fluids compared to normally-deposited coals could be explained by the conversion of dominant Sn
34 species from Sn (II)-S to Sn (IV)-O under the influence of oxidative magma, which favors the
35 enrichment of heavier Sn isotopes in Sn (IV)-O due to its shorter bond length. This study shows
36 that Sn isotope ratios are useful tools for investigating Sn geochemical behavior in different Earth
37 reservoirs and during redox sensitive processes.

38 **Key words:** tin; tin isotopes; magma intrusion; binary mixing models; redox states

39

40 **1. Introduction**

41 Magmatic intrusion is a commonly occurred process in coal deposit and severely affects the
42 safety and productivity of coal mining (Finkelman et al., 1998; Querol et al., 1997). The intrusions
43 are highly firm and thus are difficult to mine through. The emplacements usually form joints and
44 fractures that may cause instabilities of initial coal roofs and walls. Furthermore, the thermal
45 energy carried by magmatic intrusions can alter coals into cokes, and release methanes and carbon
46 monoxides, causing risks of spontaneous combustion and outbursting (Golab and Carr, 2004).

47 Tin (Sn) could be used as a proxy for magmatic intrusion in coal deposit. Sn is a
48 redox-sensitive element with two main oxidized states Sn (II) and Sn (IV) and able to behave as a
49 chalcophile or lithophile element in magmatic intruded coal deposits (Qu et al., 2016; Teng et al.,
50 2017; Wang et al., 2018; Witt-Eickschen et al., 2009). Despite the generally low concentration of
51 Sn in coals (2 µg/g, Dai et al., 2012; Ketris and Yudovich, 2009), magmatic activities might
52 deliver variable amounts of Sn from melts, magmatic-differentiated hydrothermal fluids into coals
53 (Haapala, 1997; Taylor and Wall, 1992). As a result, Sn levels in magmatic-affected coals could be
54 elevated by several folds compared to the background coals (Dai et al., 2013, 2012; Sun et al.,
55 2010). However, the sources and migration pathways of Sn in magmatic-affected coal deposits are
56 still rarely investigated.

57 High-precision measurement of Sn stable isotope ratios in last decade offers a new way to
58 constrain the sources and geochemical processes of Sn. Tin has 10 stable isotopes with a relatively

59 large mass difference: ^{112}Sn , ^{114}Sn , ^{115}Sn , ^{116}Sn , ^{117}Sn , ^{118}Sn , ^{119}Sn , ^{120}Sn , ^{122}Sn and ^{124}Sn . Up to
60 now, only few studies reported Sn isotopic compositions. Significant isotope fractionations up to
61 0.40‰ in $\delta^{124/116}\text{Sn}$ have been observed in a laboratory-controlled electrolytic plating experiment
62 between Sn (II) and Sn (IV) ions (Wang et al., 2019). Magmatic differentiation has been suggested
63 to cause small, but significant Sn isotope fractionation as well. For example, Creech et al. (2017)
64 found ~0.3‰ difference in $\delta^{122/118}\text{Sn}$ between basalt and granite during the differentiation of
65 magmas. Even larger Sn isotope fractionation was observed by Yao et al. (2018) where the later
66 formed stannite ($\text{Cu}_2\text{FeSnS}_4$) is lighter than the earlier formed cassiterite (SnO_2) by ~2‰ in
67 $\delta^{124/116}\text{Sn}$. The distinguishable isotope signatures of different magmatic components and the
68 discerned fractionation trajectories during magmatic differentiation processes provide an
69 opportunity to trace the Sn behavior in magmatic-affected coals.

70 Here, a series of coal samples taken from a magmatic-affected coal deposit in China were
71 measured for their Sn isotope ratios along with elemental and petrographic parameters. Our
72 objectives are 1) to investigate whether Sn isotope ratios are distinguishable among coals affected
73 by varying degrees of magmatic intrusion, 2) to trace Sn behaviors in magmatic-affected coals,
74 and 3) to quantify the contributions of Sn from different sources.

75

76 **2. Materials and Methods**

77 **2.1 Study area**

78 Zhuji Coalmine locates in the north of Huainan Coalfield, China (Fig. 1). The coal seams
79 deposited in the Permo-Carboniferous Period, and the fractures and faults highly developed in the
80 coalmine. The largest fault is the NWW-NW extending Minglongshan Fault, which cut through
81 the coalmine from the east to the west. The faults were considered to be formed in the Indosinian
82 orogeny at 257-205 Ma (Song et al., 2005; Yang et al., 2012).

83 The coal seams in Zhuji Coalmine suffered from multi-stage magmatic intrusions, forming a
84 series of magma intruded coals (Sun et al., 2010; Yang et al., 2012). Fig 1C graphically presented
85 the general area of the magmatic emplacement. According to the U-Pb dating of zircons, the
86 magma intrusion mainly occurred in the Late Yanshanian stage (~110 Ma). The pre-developed
87 faults and fractures acted as effective pathways for the magmatic intrusion (Chen et al., 2014;

88 Yang et al., 2012).

89 2.2 Samples and reagents

90 Twelve samples were taken from coal seams of Zhuji Coalmine (Sun et al. 2010). The sample
91 locations and other detailed information were respectively shown in Fig 1 and Table 1. More
92 details about the stratigraphic characteristics and the intrusion of the coal seams were described in
93 the study of Sun et al. (2010) and Yang et al. (2012). An international coal standard SARM 20
94 (CRPG) was used in this study for sample digestion recovery verification.

95 Teflon Savillex® beakers were used throughout the experiment for sample processing and
96 storage. The beakers were previously cleaned by aqua regia (HNO₃: HCl=1:2, analytical grade)
97 and HF (50%, v/v), and further rinsed by ultrapure water from a Milli-Q system (Millipore,
98 France). For the whole sample processing and measurement, the bi-distilled HNO₃ and HCl, and
99 ultrapure H₂O₂ and HF (Merck, German) were used.

100

101 2.3 Mineralogical and Elemental analysis

102 The mineral composition of the samples was determined by an X-ray diffractometer (XRD,
103 Philips X'Pert PRO, Japan, with diffraction angle ranging between 3° and 60°. The mineral phases
104 were identified by the Jade 6.0 (Philips, Netherland).

105 The ash yield (A_d) of the coals was analyzed following the GB/T211-2008. 0.05g of
106 air-dried coal powder (200 mesh) was taken with a porcelain boat and ashed in the Muffle furnace.
107 The heating temperature was set to 815°C and kept for 2hs. After the heating procedure, the A_d
108 was calculated as following:

$$109 \quad A_d = m_a / m_i * 100\%,$$

110 where the m_a was the mass of the ash yield after the furnace and the m_i the initial mass of the coal.

111 The concentrations of major elements (Na, K, Ca, Mg, Fe, Al, Si and Ti) and trace elements
112 (La, Th, U, Pb, Zn, Cd, Sb, Rb, Cr, Mn, Cu, Sr, Ba, Nb, Mo, Ni, Co, V and Zr) were measured by
113 X-ray fluorescence and high resolution-inductively coupled plasma mass spectrometry
114 (Element-XR, Thermo-Scientific Inc.), respectively. For the HR-ICP-MS measurement, 0.05 g of
115 each sample was digested by acid mixture of HNO₃: H₂O₂: HF (8mL: 2mL: 2mL) within a
116 microwave system (Mars 5, CEM Inc.). The heating program was set as 120°C-15min-1200W,
117 150°C-10min-1200W and 190°C-30min-1800W. The digested solution was cooled down to room

118 temperature and transferred to the Savillex beakers. Then, the sample solutions were dried at 70°C
119 and re-dissolved in 10 mL 2% HNO₃ and 0.01% HF (v/v) before trace element measurement and
120 subsequent Sn purification by column chromatography. An indium (In) internal standard
121 (Lot#56875, Merck Inc.) was used to monitor the signal stability during the HR-ICP-MS analysis.

122

123 2.4 Tin stable isotope analysis

124 A two-step chromatographic method modified from Wombacher et al. (2003) and Yi et al.
125 (1995) was adapted to separate Sn from digested solutions (Table 2). An anion-exchange resin AG
126 1-X8 (100-200 mesh, Bio-rad Inc.) was firstly employed to separate Sn and Cd from major
127 elements of the digested solutions using a 10 mL polypropylene column (Bio-rad Inc.). Before the
128 sample loading, the digested solution was dried at 70°C and then re-dissolved by 5mL 3M HCl. In
129 addition, 100µL HF (3M, v/v) was added into the re-dissolved solution to prevent Sn hydrolysis.
130 The final eluents of AG 1-X8 were collected for the following TRU-spec resin separation
131 (#TRU-B50-A, 100-150µm, Eichrom Inc.). After the two-step chromatographic purification, the
132 final eluents were concentrated and re-dissolved into a 3 mL solution for the isotope measurement
133 by using a MC-ICP-MS (Neptune, Thermo Finnigan). Before the isotope measurement, a Sn
134 recovery verification was performed on the HR-ICP-MS. A coal standard SARM 20 was
135 processed along with the samples. The Sn recovery for SARM 20 after digestion and
136 chromatographic purification was better than 90%. The procedural blanks were negligible
137 compared to the Sn mass in standards and samples.

138 The stable isotope ratios of Sn were determined by a multi-collector inductively coupled
139 plasma mass spectrometer (MC-ICP-MS, Neptune, Thermo Finnigan) at Geosciences
140 Environnement Toulouse Laboratory. The instrument equipped with a Jet sample cone and H
141 skimmer cone. A PFA micro-nebulizer and Scott type double pass spray chamber were used to
142 introduce the sample solutions. The sample uptake rate was approximately 100 µL/min. The
143 sample solutions were kept at 30 ng/mL doped with 60 ng/mL of Sb, which generated ~1V signal
144 intensity of ¹²⁰Sn. Six Sn isotopes (¹¹⁶Sn, ¹¹⁷Sn, ¹¹⁸Sn, ¹¹⁹Sn, ¹²⁰Sn and ¹²²Sn), and two Sb isotopes
145 (¹²¹Sb, ¹²³Sb) and ¹²⁶Te were simultaneously collected by L4-H4 Faraday cups. One sample run
146 consisted of 35 measurements with 8s integration time of each scan.

147 Mass bias of the MC-ICP-MS was corrected by an internal NIST 3102a Sb standard and

148 NIST 3161a Sn standard-sample bracketing method. For the internal correction, an exponential
 149 law was used to obtain the mass bias factor β (equation 1) which was then applied to correct the
 150 measured Sn isotope ratios:

$$\beta = \frac{\ln(r_{Sb}/R_{Sb})}{\ln(^{123}Sb/^{121}Sb)} \quad (1)$$

151
 152 where the r_{Sb} and R_{Sb} respectively refer the true and observed isotopic ratios of internal Sb
 153 standard solution. The $^{123}Sb/^{121}Sb$ refers the mass ratio of two Sb isotopes. A natural abundance
 154 ratio of $^{123}Sb/^{121}Sb = 0.7480$ proposed by Meija et al. (2016) was used to represent the true ratio of
 155 the Sb standard solution. The corrected Sn isotope ratios of the samples were expressed as
 156 $\delta^{120/118}Sn$ (‰).

$$\delta^{120/118}Sn_{sample} = \frac{r_{120/118Sn}^{sample} - r_{120/118Sn}^{standard}}{r_{120/118Sn}^{standard}} \times 10^3 \text{ (‰)} \quad (2)$$

157
 158 where the r^{sample} and $r^{standard}$ represented the Sn isotopic ratios of the samples and standard NIST
 159 3161a Sn solution. For the measured isotopic variations, ^{120}Sn and ^{118}Sn were selected for the
 160 calculation because they were the most abundant Sn isotopes with the highest precision. The
 161 one-day continuous measurement of the isotope ratios of the NIST standard was shown in Fig.2. A
 162 long-term reproducibility for of $\delta^{120/118}Sn$ of the SARM 20 was 0.07 ‰ (2σ , $n=17$, Fig 2).

163

164 2.5 Mathematic simulation

165 Based on a binary mixing model, the Sn input from two source end-members were simulated.
 166 The simulation was performed by a Monte Carlo approach used by Jiskra et al. (2015). A
 167 Pseudo-Random Function ($i=1$ to 1000) was settled as the iteration number and the computational
 168 processes were operated as the following equations:

$$\sum_{j=1}^n f_j \times I_j = I_{sample} \quad (3)$$

169

$$\sum_{j=1}^n f_j = 1 \quad (4)$$

170

171 where j referred to the Sn source members, f_j referred to the Sn fraction of each source, I_j referred
172 to Sn isotope values of each source member, I_{sample} referred to the $\delta^{120/118}\text{Sn}$ measured for each
173 sample. Isotope values of I_j were taken from the samples which showed the most positive or
174 negative isotope variations. The computation was performed on the platform of Matlab (R2016b,
175 Mathworks).

176

177 **3. Results and discussion**

178 3.1 Mineralogical analysis

179 The XRD spectrums of coal samples were presented in Fig.3. For easy comparison, the
180 samples were re-ordered based on their intensity ratios of the highest peak and the mean spectrum
181 background (S/N). The highest S/Ns were found in coal samples #12-5-7, #15-5-7 and #16-4-5,
182 with a value of 93.02, 15.22 and 14.01, respectively. For the samples with high S/N, quartz was
183 dominant mineral followed by biotite, muscovite, amesite and chamosite. The lowest S/N value
184 was seen in samples #15-5-11 (2.44). Their dominant minerals were kaolinite followed by sulfide
185 and carbonates. The varied mineral assemblage between the high S/N samples and the low S/N
186 sample suggested that the samples experienced different forming processes. The high S/N sample
187 were probably intruded by magmatic materials, because the biotite, muscovite, amesite and
188 chamosite were common minerals found in metamorphosed or igneous rocks (Aarnes et al., 2011;
189 Andreani et al., 2013; Dai et al., 2008; Dai and Chou, 2007), whereas the low S/N samples were
190 commonly found in the normally deposited coals (Chou, 2012; Pinetown et al., 2007).

191 Ash yield (A_d) was a common index to evaluate the non-volatile mineral proportions of the
192 samples (mainly alumino-silicates) (Table 1). Sample #12-7-5, #15-5-7 and #16-4-5, showed the
193 highest A_d (78.53% for #12-7-5, 51.87% for #15-5-7 and 46.85% for 16-4-5), according with their
194 S/Ns. In contrast, sample with the lowest S/N ratios showed the lowest ash yield (10.53% for
195 #15-5-11). The high correlation between the ash yield and S/N was probably caused by the
196 magmatic intrusions of the coal deposit, as magma intrusions usually accompanied with a
197 significantly increase of silicates.

198 3.2 Elemental analysis

199 3.2.1 The high mineral content samples

200 Three samples (#12-7-5, #16-4-5 and #15-5-7) would be mainly discussed in the following
201 elemental concentration comparison as they were the most represented high mineral content
202 samples. Relative to the elemental backgrounds of Huainan coal and Chinese coal averages (Chen
203 et al. (2014); Dai et al. (2012)), higher levels of Na, Mg, Al, Si, Ba, Sr, Cr, Mn, Nb, Th, Rb and Zr
204 were found in the three samples ($C_{\text{this study}} >$ both C_{Huainan} and C_{Chinese}), whereas Fe was depleted
205 (Fig.4). However, compared with the other samples of this study, the highest Fe levels were shown
206 in the three samples. Among the enriched element collection, Na, Al, Si were elements according
207 with the higher proportions of quartz and minor minerals in the samples; Nb, Zr, Sr, Ba, Rb and La
208 were geochemically incompatible elements, which usually concentrated in the highly
209 differentiated magma melts or fluids; Mn and Rb were the elements with the highest enrichment
210 coefficient (ECs) in this study, 2.8-16.5 of Rb and 1.9-4.6 of Mn. In the studies of magmatic
211 intruded coal deposits (Golab and Carr., 2004; Querol et al., 1997), intensely increase of Mn in
212 coals (Table 1S, Supplementary Material) was usually interpreted as precipitation of carbonates,
213 which were caused by reactions of CO and CO₂ from magmatic fluids altered coals. Rb, Sr, Ba, Ca
214 and Mg were usually the main cations of the carbonates and they were able to substitute with each
215 other. Furthermore, in #15-5-7, chalcophile elements of Pb, Zn, Cd, Sb, Cu and Mo were more
216 enriched than that of #12-7-5 and #16-4-5 and other samples. The differences of elemental
217 associations between #12-7-5, #16-4-5 and #15-5-7 demonstrated that #15-5-7 experienced a more
218 S-rich intrusion than #12-7-5 and #16-4-5. Therefore, it could be concluded that #12-7-5, #16-4-5
219 and #15-5-7 affected by the magmatic intrusions, which were more likely the magmatic
220 hydrothermal fluids than the melts, and the fluids intruded #15-5-7 were more reduced than that
221 intruded #12-7-5 and #16-4-5.

222 To make a further explanation of why it was more probably of the hydrothermal fluids
223 intrusion than magmatic melts, an alumina saturation index A/CNK (molar Al₂O₃/
224 (CaO+Na₂O+K₂O)) was introduced (Clarke, 2019; Gao et al., 2016). Basing on the published data
225 (Yang et al., 2012), we calculated the A/CNKs of the intrusive melt of Zhuji coalmine and
226 compared the values with the coal samples. The A/CNKs of the three samples with the highest
227 possibilities of magma intrusion were 3.87 (#12-7-5), 7.08 (#16-4-5) and 8.50 (#15-5-7), while the
228 intrusive melt ranged between 0.60-1.41, comparable to a peraluminous granite (Clarke, 2019,
229 1981; Pérez-Soba and Villaseca, 2010). Since the much higher A/CNKs of the coals than the

230 intrusive melts, the samples were not likely directly intruded by magmatic melts, but the
231 hydrothermal fluids. This was also supported by Clarke (1981), who considers that rock samples
232 with $A/CNK \gg 1$ could be caused by the interaction with hydrothermal fluids from silicate melts.

233 3.2.2 The low mineral content samples

234 Relative to the average of Huainan coals (22.1%, Chen et al., 2011), six samples showed
235 lower A_d (10.53-21.99%). Among the six samples, #15-5-11 showed the lowest A_d of 10.53%,
236 demonstrating that coal organics dominated in the sample. #16-4-4 showed the highest ash yield
237 of the six samples, probably owing to an enriched iron minerals (Fe 1.22%).

238 According to the mineralogy and elemental analysis, it was observed that the A_d and Mn level
239 were sensitive indicators to reflect variations of magmatic impact on the samples. Therefore, we
240 considered that three samples were severely affected by magmatic intrusions (#12-7-5, #16-4-5
241 and #15-5-7, $A_d > 50\%$ and $Mn > 200 \mu\text{g/g}$), while the other samples were less possible affected by
242 the intrusions.

243

244 3.3. Concentration and isotope variations of Sn

245 Sn levels and $\delta^{120/118}\text{Sn}$ values of the studied coals were listed in Table 1. The Sn levels
246 ranged between 0.94 and 4.48 $\mu\text{g/g}$, with an average of 2.06 $\mu\text{g/g}$. High Sn levels were found in
247 coals with the highest A_d (#12-7-5 4.48 $\mu\text{g/g}$, #15-5-7 2.28 $\mu\text{g/g}$ and #16-4-5 2.12 $\mu\text{g/g}$), while the
248 lowest Sn level was found in sub-bituminous coal #15-5-11 (0.94 $\mu\text{g/g}$) with the lowest A_d .
249 $\delta^{120/118}\text{Sn}$ of the coals ranged from -0.06‰ to 0.22‰ (± 0.07 , 2σ).

250 Below we propose two major mechanisms to explain the observed variations of Sn isotopes
251 in coals: 1) a mixing of Sn isotope from different sources; 2) Sn isotope fractionation caused by
252 redox changes. With the current data, we were unable to identify which mechanism was dominant.
253 However, it was likely that both mechanisms were responsible for the Sn isotope variation
254 observed.

255

256 3.4 Possible contributing sources of Sn

257 As was shown in Fig.5, a linear correlation could be fitted between $1/\text{Sn}$ concentrations and
258 $\delta^{120/118}\text{Sn}$ values ($r=0.64$). This correlation suggested that the Sn isotope variations in the coals
259 might be controlled by the mixing of two end-members with different $\delta^{120/118}\text{Sn}$. The two

260 end-members were most likely the Sn carried by the intruded magmatic hydrothermal fluids and
261 the Sn from the original deposited coals. In this study, the magmatic affected samples (#12-5-7,
262 #15-5-7 and #16-4-5) had higher $\delta^{120/118}\text{Sn}$ values (0.09-0.22‰), and the most represented coal
263 samples (#15-5-11 and #16-4-4) had the lowest $\delta^{120/118}\text{Sn}$ variations (-0.04‰ and -0.06‰).

264 Based on the mineralogical and elemental evidences, the samples with the higher $\delta^{120/118}\text{Sn}$
265 values were affected more by magmatic-intrusion, and thus a higher fraction of magmatic-derived
266 Sn was expected in these samples. As a chalcophile and lithophile element, Sn showed the highest
267 affinities with either oxygen or sulfur at different redox states. According to the study of
268 Badullovich et al. (2019), the species of Sn depended on the levels of $f(\text{O}_2)$ of the intruded
269 magmatic materials. In coal deposits, Sn could associated with alumino-silicates, sulfide minerals
270 (mainly pyrite (FeS)) or coal organic matters (Qu et al., 2016). In this study, the $f(\text{O}_2)$ of #12-7-5
271 and #16-4-5 were obviously higher than #15-5-7. Thus, the Sn in #12-7-5 and #16-4-5 were most
272 likely in Sn(IV)-O form, whereas the Sn in #15-5-7 more possible occurred as Sn(II)-S. In contrast,
273 the samples with the lowest $\delta^{120/118}\text{Sn}$ ratios (#15-5-11 and #16-4-4) were unlikely affected by
274 magmatic-intrusion as they had lower A_d and mineral contents. Due to the studies of Sn modes of
275 occurrence in coals, the Sn in low A_d coals could either associated with the coal organics to form
276 functional groups or associated with sulfide minerals, such as FeS and $\text{Cu}_2\text{FeSnS}_3$. In our study,
277 the Sn in #15-5-11 was mostly likely associated with the coal organic, while the Sn in #16-4-4
278 more tended to associate with sulfide minerals, as there was a high level of Fe (1.22%).

279 The Sn isotope variations of the coals in this study was further compared with other
280 published Sn isotope ratios (Fig. 6). Sn isotope variations of magmatic rocks were more positive
281 with respect to the samples from other geochemical reservoirs, indicating an enrichment of heavy
282 Sn isotopes in earth mantle and crust. The most positive coal $\delta^{120/118}\text{Sn}$ (#12-7-5 and #16-4-5)
283 corresponded closely to the isotopic ranges of the highly-evolved acidic magmatic rocks, which
284 was supported by Yang et al. (2012). Sample #15-5-11 and #16-4-4, which had the most negative
285 $\delta^{120/118}\text{Sn}$ variations, were observed on the upper limit of the isotopic range of sulfide-associated
286 Sn minerals ($\text{Cu}_2\text{FeSnS}_3$) (-0.06 to -0.56‰). Since the Sn in coals could either associated with the
287 coal organic sulfur or sulfide minerals, the negative $\delta^{120/118}\text{Sn}$ in #15-5-11 and #16-4-4 may
288 therefore indicate a partial coordination of Sn (II) by the coal organic and sulfide minerals
289 respectively.

290 A binary mixing model was applied to estimate the contributions of the two end-members
 291 (magmatic hydrothermal fluids and original coal deposit) to the Sn budget in coals. In this model,
 292 published $\delta^{120/118}\text{Sn}$ of granite was used to represent the Sn end-member in magmatic
 293 hydrothermal fluids (Fig. 6), since it was considered that no isotope fractionation occurred during
 294 Sn crystallization of silicates (Badullovich et al., 2017). For the $\delta^{120/118}\text{Sn}$ of the other end-member
 295 (coal organics), the upper limit of stannite isotope variation (Fig. 6), which was close to the
 296 isotope variation of #16-4-4 and #15-5-11, was used to represent the Sn coordinated to S. Based
 297 on the following equations (5) and (6), Sn contributions by the two end-members in each coal
 298 samples were calculated. The detailed calculations were listed in the Supplementary Material
 299 Table S2 (csv file).

$$f_1 \times \delta^{120/118}\text{Sn}_1 + f_2 \times \delta^{120/118}\text{Sn}_2 = \delta^{120/118}\text{Sn}_{\text{sample}} \quad (5)$$

300

$$f_1 + f_2 = 1 \quad (6)$$

301 According to the simulation, the Sn input carried by the magmatic sourced hydrothermal
 302 fluids contributed 86% ($\pm 9.5\%$, 1σ) of the Sn in the sample with the most positive isotope
 303 variation (#12-7-5), while only 14% ($\pm 11.5\%$, 1σ) of the Sn in the sample from the coal organics
 304 (#15-5-11). The detailed calculation results could be seen in the Supporting material.

305

306 3.5 Isotope variations of Sn caused by redox changes

307 In addition to the mixing of Sn from two geochemical reservoirs, changes in redox states of
 308 Sn in coals could be responsible for the isotope variation of this study as well, since redox changes
 309 between Sn (II) and Sn (IV) had been proved to cause small, but detectable isotope fractionation
 310 (Wang et al. 2019). In this study, an oxidation of magmatic affected coal seams probably happened
 311 because comparing to the reductive coal deposition environment (usually Sn occurred as Sn (II)-S),
 312 the intruded magmatic hydrothermal fluids could be more oxic when it had a high oxygen fugacity
 313 ($f(\text{O}_2)$). According to the calculation by Badullovich et al. (2017), Sn could occur as Sn (IV) in
 314 magmatic liquids at $f(\text{O}_2)$ of Fayalite-Magnetite-Quartz (FMQ) and temperature of $\sim 1200^\circ\text{C}$. In
 315 this study, since the temperature of hydrothermal fluids partitioning from melts was usually lower
 316 than 800°C , and trace amount of biotite and muscovite (usually Fe (III) rich) were detected in the
 317 hydrothermal fluid impacted samples, the $f(\text{O}_2)$ of the samples were apparently higher than the

318 estimation of Badullovich et al. Therefore, the hydrothermal fluids were able to transfer the initial
319 organic associated Sn (II) to oxidized Sn (IV) and contribute isotope shifts of Sn isotopes in this
320 study.

321 To evaluate redox condition of the coal samples, a series of well-developed paleo-redox
322 proxies, $V/(V+Ni)$, Mn/Cr and V/Cr (Hatch and Leventhal, 1992; Jones and Manning, 1994; Nico
323 et al., 2009; Rimmer, 2004), were examined in this study. High V/Cr ratios (>2) in coals were
324 thought to empirically indicate dysoxic conditions, and $V/(V+Ni)$ (>0.2) predict dysoxic to euxinic
325 conditions. Mn and Cr were considered as a pair of elements with reverse behaviors of solubility
326 in both oxic and reductive conditions. It was usually considered that the higher ratios of Mn/Cr ,
327 the more reductive the condition was. As shown in Fig. 7A, the samples were re-ordered by their
328 drill hole locations. A profile of $\delta^{120/118}Sn$ of the samples were compared with the three
329 paleo-redox proxies (Fig 7A). They were also compared with A_d , Na and Si (Fig 7B), which were
330 characteristic properties for magmatic intrusions. It was striking to find that all three redox proxies
331 indicated relatively more oxic conditions for the samples with the most positive $\delta^{120/118}Sn$ (#12-7-5
332 and #16-4-5) than the less positive $\delta^{120/118}Sn$ (#15-5-7), and the samples with the most negative
333 $\delta^{120/118}Sn$ (#15-5-11 and #16-4-4) (Fig. 7A). Furthermore, positive correlations were found
334 particularly between the most positive $\delta^{120/118}Sn$ samples and the contents of A_d , Na and Si (Fig.
335 7B), which were characteristic properties for magmatic intrusions. Combing the two sets of
336 evidences, we suggested that the magmatic hydrothermal fluid intrusion into coal seams might
337 have shifted the redox conditions of coals to be more oxic, and also the redox states of the Sn in
338 the coals.

339 The magmatic hydrothermal fluids intrusion could change the redox states of Sn in coals
340 through a Sn re-mobilization process (Golab and Carr, 2004). Carrying with large amounts of
341 thermal energy and mineral contents, the intruded fluids were able to alter the coals by either
342 pyrolyzation or mineral contamination (Dai et al., 2004). The former could partially decompose
343 the coal organic matters and sulfide minerals, leading to a volatilization of the associated Sn. The
344 latter demonstrated that a material exchange took place between the coals and the fluids, and
345 partial Sn of the coals could be leached out by the fluid. Hence, a Sn re-mobilization happened
346 while the coals was intruded by a magmatic hydrothermal fluids.

347 Basing on the analysis of $\delta^{120/118}Sn$ variations of the samples and Sn geochemistry in

348 hydrothermal fluid affected coals, we proposed a conceptual model to explain the mechanism of
349 the possible $\delta^{120/118}\text{Sn}$ variations. As was discussed above, the chemical species of Sn highly
350 depended on the levels of $f(\text{O}_2)$. In oxidizing condition, Sn usually associated with O in Sn(IV)-O,
351 while under reducing condition, Sn was in Sn (II) and had a high affinity with S. Since Sn(IV)-O
352 had much shorter bond length ($\sim 2.18\text{\AA}$) than Sn(II)-S ($\sim 2.48\text{\AA}$), the heavier Sn isotopes were more
353 likely enriched in Sn(IV)-O species with shorter and stiffer chemical bonds (Badullovich et al.,
354 2017; Bigeleisen and Mayer, 1947; Gürel et al., 2011; She et al., 2019; Yao et al., 2018). In this
355 study, since the organic matters of #15-5-11 and #16-4-4 accounted for 80% to 90% of the total
356 coals, most of the Sn in the samples should associate with the reduced organic matters and thus a
357 more negative isotope shift of $\delta^{120/118}\text{Sn}$ was observed. For #12-7-5 and #16-5-4, as they were
358 affected by magmatic hydrothermal fluids with high $f(\text{O}_2)$, the Sn of the initial coals could be
359 either oxidized to Sn (IV) or leached out, resulting in an enrichment of heavier Sn isotopes in the
360 residue phase. For sample #15-5-7, because it was intruded by a S-rich hydrothermal fluid, a
361 negative $\delta^{120/118}\text{Sn}$ isotope shift relative to #12-7-5 and #16-4-5 could be observed.

362 Summarily, the mixing of two end-members and the redox changes that could both
363 fractionate Sn isotopes were proposed to explain the isotope variations of the coals. However,
364 considering the similar Sn content (ppm level) in coals and magma fluid (e.g. MORB) and the lack
365 of direct evidence, we were not able to distinguish the effect of redox change from magmatic input
366 on Sn isotope variation at this stage, further systematic study was thus needed to better constrain
367 Sn isotope fractionation during hydrothermalism.

368

369 **4. Conclusions**

370 In this study, Sn stable isotope variations in twelve coals with various magmatic-affected
371 degrees from a coal deposit of China vary from -0.06 to 0.22‰ in $\delta^{120/118}\text{Sn}$. The Sn stable isotope
372 variations demonstrate clear difference between the magmatic affected samples (0.20 to 0.22‰)
373 and the normally deposited coals (-0.04 to -0.06‰). Two possible interpretations are suggested to
374 explain the isotopic variation of the samples. The first, the isotope variation is attributed to a
375 mixture of magmatic hydrothermal fluids and coal deposits with different Sn isotope ratios, as
376 demonstrates by the linear relationship between Sn and its isotopes in a mixing diagram. The

377 second, an oxidation of the coal seams probably take place when they are intruded by the
378 magmatic hydrothermal fluids. In fact, the higher oxidation states of the intruded coals leads to an
379 enrichment of heavy Sn isotopes. This enrichment can be roughly explained by the relatively
380 shorter bond length of Sn (IV)-O than Sn (II)-S. Both of the two geochemical processes were
381 considered responsible for the variation determined in this study. Finally, our work shows that Sn
382 isotope ratios are useful tools for investigating Sn geochemical behavior in different Earth
383 reservoirs and during redox-sensitive processes.

384 **Acknowledgement**

385 This study was supported by the Natural Science Foundation of China (No. 41625012,
386 U1612442, 41561134017 and 41961144028) and National Key Research and Development
387 Program of China (No. 2019YFC1804400). We acknowledge financial and logistic support from
388 the Laboratoire de Géosciences Environnement Toulouse, Observatoire Midi-Pyrénées,
389 CNRS/IRD/Université Paul Sabatier Toulouse III, France.

390

391 **References**

- 392 Aarnes, I., Svensen, H., Polteau, S., Planke, S., 2011. Contact metamorphic devolatilization of shales in
393 the Karoo Basin, South Africa, and the effects of multiple sill intrusions. *Chem. Geol.* 281, 181–
394 194.
- 395 Andreani, M., Daniel, I., Pollet-Villard, M., 2013. Aluminum speeds up the hydrothermal alteration of
396 olivine. *Am. Mineral.* 98, 1738–1744.
- 397 Badullovich, N., Moynier, F., Creech, J., Teng, F.F.-Z., Sossi, P.A.P.A., 2017. Tin isotopic
398 fractionation during igneous differentiation and Earth's mantle composition. *Geochemical*
399 *Perspect. Lett.* 24–28. <https://doi.org/10.7185/geochemlet.1741>
- 400 Bigeleisen, J., Mayer, M.G., 1947. Calculation of Equilibrium Constants for Isotopic Exchange
401 Reactions. *J. Chem. Phys.* 15, 261–267. <https://doi.org/10.1063/1.1746492>
- 402 Chen, J., Liu, G., Li, H., Wu, B., 2014. Mineralogical and geochemical responses of coal to igneous
403 intrusion in the Pansan Coal Mine of the Huainan coalfield, Anhui, China. *Int. J. Coal Geol.* 124,
404 11–35. <https://doi.org/10.1016/j.coal.2013.12.018>
- 405 Chen, J., Liu, G., Jiang, M., Chou, C.-L., Li, H., Wu, B., Zheng, L., Jiang, D., 2011. Geochemistry of
406 environmentally sensitive trace elements in Permian coals from the Huainan coalfield, Anhui,
407 China. *Int. J. Coal Geol.* 88, 41–54. <https://doi.org/10.1016/j.coal.2011.08.002>
- 408 Chou, C.L., 2012. Sulfur in coals: A review of geochemistry and origins. *Int. J. Coal Geol.* 100, 1–13.
409 <https://doi.org/10.1016/j.coal.2012.05.009>
- 410 Clarke, D.B., 2019. The Origins of Strongly Peraluminous Granitoid Rocks. *Can. Mineral.*
411 *canmin--1800075.*
- 412 Clarke, D.B., 1981. The mineralogy of peraluminous granites: a review. *Can. Mineral.* 19, 3–17.

413 Creech, J.B., Moynier, F., Badullovich, N., 2017. Tin stable isotope analysis of geological materials by
414 double-spike MC-ICPMS. *Chem. Geol.* 457, 61–67.
415 <https://doi.org/10.1016/j.chemgeo.2017.03.013>

416 Dai, S., Chou, C.-L., 2007. Occurrence and origin of minerals in a chamosite-bearing coal of Late
417 Permian age, Zhaotong, Yunnan, China. *Am. Mineral.* 92, 1253–1261.

418 Dai, S., Li, D., Ren, D., Tang, Y., Shao, L., Song, H., 2004. Geochemistry of the late permian No. 30
419 coal seam, Zhijin coalfield of southwest China: influence of a siliceous low-temperature
420 hydrothermal fluid. *Appl. Geochemistry*, 19(8), 0-1330.

421 Dai, S., Ren, D., Chou, C.-L., Finkelman, R.B., Seredin, V. V, Zhou, Y., 2012. Geochemistry of trace
422 elements in Chinese coals: a review of abundances, genetic types, impacts on human health, and
423 industrial utilization. *Int. J. Coal Geol.* 94, 3–21.

424 Dai, S., Tian, L., Chou, C.-L., Zhou, Y., Zhang, M., Zhao, L., Wang, J., Yang, Z., Cao, H., Ren, D.,
425 2008. Mineralogical and compositional characteristics of Late Permian coals from an area of high
426 lung cancer rate in Xuan Wei, Yunnan, China: Occurrence and origin of quartz and chamosite.
427 *Int. J. Coal Geol.* 76, 318–327.

428 Dai, S., Zhang, W., Seredin, V.V., Ward, C.R., Hower, J.C., Song, W., Wang, X., Li, X., Zhao, L.,
429 Kang, H., Zheng, L., 2013. Factors controlling geochemical and mineralogical compositions of
430 coals preserved within marine carbonate successions: a case study from the Heshan Coalfield,
431 southern China. *Int. J. Coal Geol.* 109, 77–100.

432 Finkelman, R.B., Bostick, N.H., Dulong, F.T., Senftle, F.E., Thorpe, A.N., 1998. Influence of an
433 igneous intrusion on the inorganic geochemistry of a bituminous coal from Pitkin County,
434 Colorado. *Int. J. Coal Geol.* 36, 223–241. [https://doi.org/Doi 10.1016/S0166-5162\(98\)00005-6](https://doi.org/Doi 10.1016/S0166-5162(98)00005-6)

435 Gao, P., Zheng, Y.-F., Zhao, Z.-F., 2016. Distinction between S-type and peraluminous I-type granites:
436 Zircon versus whole-rock geochemistry. *Lithos* 258, 77–91.

437 Golab, A.N., Carr, P.F., 2004. Changes in geochemistry and mineralogy of thermally altered coal,
438 Upper Hunter Valley, Australia. *Int. J. Coal Geol.* 57, 197–210.
439 <https://doi.org/10.1016/j.coal.2003.12.011>

440 Gürel T, Sevik C, Çağın T. Characterization of vibrational and mechanical properties of quaternary
441 compounds Cu_2ZnSnS_4 and $Cu_2ZnSnSe_4$ in kesterite and stannite structures. *Physical Review B*,
442 2011, 84: 205201.

443 Haapala, I., 1997. Magmatic and Postmagmatic Processes in Tin-mineralized Granites: Topaz-bearing
444 Leucogranite in the Eurajoki Rapakivi Granite Stock, Finland. *J. Petrol.* 38, 1645–1659.
445 <https://doi.org/10.1093/petroj/38.12.1645>

446 Hatch, J.R., Leventhal, J.S., 1992. Relationship between inferred redox potential of the depositional
447 environment and geochemistry of the Upper Pennsylvanian (Missourian) Stark Shale Member of
448 the Dennis Limestone, Wabaunsee County, Kansas, USA. *Chem. Geol.* 99, 65–82.

449 Jiskra, M., Wiederhold, J.G., Skyllberg, U., Kronberg, R.-M., Hajdas, I., Kretzschmar, R., 2015.
450 Mercury deposition and re-emission pathways in boreal forest soils investigated with Hg isotope
451 signatures. *Environ. Sci. Technol.* 49, 7188–7196.

452 Jones, B., Manning, D.A.C., 1994. Comparison of geochemical indices used for the interpretation of
453 palaeoredox conditions in ancient mudstones. *Chem. Geol.* 111, 111–129.

454 Ketris, M.P., Yudovich, Y.E., 2009. Estimations of Clarkes for Carbonaceous biolithes: World
455 averages for trace element contents in black shales and coals. *Int. J. Coal Geol.* 78, 135–148.

456 Meija, J., Coplen, T.B., Berglund, M., Brand, W.A., De Bièvre, P., Gröning, M., Holden, N.E., Irrgeher,

457 J., Loss, R.D., Walczyk, T., Prohaska, T., 2016. Isotopic compositions of the elements 2013
458 (IUPAC Technical Report). *Pure Appl. Chem.* 88, 293–306.
459 <https://doi.org/10.1515/pac-2015-0503>

460 Nico, P.S., Kumfer, B.M., Kennedy, I.M., Anastasio, C., 2009. Redox dynamics of mixed metal (Mn,
461 Cr, and Fe) ultrafine particles. *Aerosol Sci. Technol.* 43, 60–70.

462 Pérez-Soba, C., Villaseca, C., 2010. Petrogenesis of highly fractionated I-type peraluminous granites:
463 La Pedriza pluton (Spanish Central System). *Geol. Acta* 8, 131–149.
464 <https://doi.org/10.1344/105.000001527>

465 Pinetown, K.L., Ward, C.R., der Westhuizen, W.A., 2007. Quantitative evaluation of minerals in coal
466 deposits in the Witbank and Highveld Coalfields, and the potential impact on acid mine drainage.
467 *Int. J. Coal Geol.* 70, 166–183.

468 Qu, Q., Liu, G., Sun, R., Kang, Y., 2016. Geochemistry of tin (Sn) in Chinese coals. *Environ. Geochem.*
469 *Health* 38, 1–23. <https://doi.org/10.1007/s10653-015-9686-z>

470 Querol, X., Alastuey, A., Lopez-Soler, A., Plana, F., Fernandez-Turiel, J.L., Zeng, R., Xu, W., Zhuang,
471 X., Spiro, B., 1997. Geological controls on the mineral matter and trace elements of coals from
472 the Fuxin basin, Liaoning Province, northeast China. *Int. J. Coal Geol.* 34, 89–109.
473 [https://doi.org/10.1016/s0166-5162\(97\)00014-1](https://doi.org/10.1016/s0166-5162(97)00014-1)

474 Rimmer, S.M., 2004. Geochemical paleoredox indicators in Devonian–Mississippian black shales,
475 central Appalachian Basin (USA). *Chem. Geol.* 206, 373–391.

476 She, J.-X., Wang, T., Liang, H.-D., Muhtar, M.N., Li, W., Liu, X., 2019. Sn isotope fractionation
477 during volatilization of Sn (IV) chloride: laboratory experiments and quantum mechanical
478 calculations. *Geochim. Cosmochim. Acta*.

479 Singh, A., Singh, V.K., Singh, R.A., 2011. Petrographical studies Vis-a-Vis Tin-bearing granitoids,
480 southern Bastar craton, India, in: *Proceeding of the 2nd International Conference Precambrian*
481 *Continental Growth and Tectonism*. pp. 103–110.

482 Song, C., Zhu, G., Liu, G., Niu, M., Chuangzhong, S., Guang, Z., Guosheng, L., Manlan, N., 2005.
483 Identification of structure and its dynamics control of Huainan coalfield. *Coal Geol. Explor.* 33,
484 11–15.

485 Sun, R., Liu, G., Zheng, L., Chou, C.-L., 2010. Geochemistry of trace elements in coals from the Zhuji
486 Mine, Huainan Coalfield, Anhui, China. *Int. J. Coal Geol.* 81, 81–96.
487 <https://doi.org/10.1016/j.coal.2009.12.001>

488 Taylor, J.R., Wall, V.J., 1992. The behavior of tin in granitoid magmas. *Econ. Geol.* 87, 403–420.
489 <https://doi.org/10.2113/gsecongeo.87.2.403>

490 Teng, F.Z., Dauphas, N., Watkins, J.M., 2017. Non-traditional stable isotopes: retrospective and
491 perspective. *Rev. Mineral. Geochemistry* 82, 1–26.

492 Wang, D., Mathur, R., Powell, W., Godfrey, L., Zheng, Y., 2019. Experimental evidence for
493 fractionation of tin chlorides by redox and vapor mechanisms. *Geochim. Cosmochim. Acta* 250,
494 209–218.

495 Wang, X., Amet, Q., Fitoussi, C., Bourdon, B., 2018. Tin isotope fractionation during magmatic
496 processes and the isotope composition of the bulk silicate Earth. *Geochim. Cosmochim. Acta* 228,
497 320–335. <https://doi.org/10.1016/j.gca.2018.02.014>

498 Wang, X., Fitoussi, C., Bourdon, B., Amet, Q., 2017. A new method of Sn purification and isotopic
499 determination with a double-spike technique for geological and cosmochemical samples. *J. Anal.*
500 *At. Spectrom.* 32, 1009–1019. <https://doi.org/10.1039/c7ja00031f>

501 Witt-Eickschen, G., Palme, H., O'Neill, H.S.C., Allen, C.M., 2009. The geochemistry of the volatile
502 trace elements As, Cd, Ga, In and Sn in the Earth's mantle: New evidence from in situ analyses
503 of mantle xenoliths. *Geochim. Cosmochim. Acta* 73, 1755–1778.

504 Wombacher, F., Rehkämper, M., Mezger, K., Münker, C., 2003. Stable isotope compositions of
505 cadmium in geological materials and meteorites determined by multiple-collector ICPMS.
506 *Geochim. Cosmochim. Acta* 67, 4639–4654. [https://doi.org/10.1016/S0016-7037\(03\)00389-2](https://doi.org/10.1016/S0016-7037(03)00389-2)

507 Yamazaki, E., Nakai, S., Sahoo, Y., Yokoyama, T., Mifune, H., Saito, T., Chen, J., Takagi, N.,
508 Hokanishi, N., Yasuda, A., 2014. Feasibility studies of Sn isotope composition for provenancing
509 ancient bronzes. *J. Archaeol. Sci.* 520, 458–467. <https://doi.org/10.1016/j.jas.2014.09.014>

510 Yamazaki, E., Nakai, S., Yokoyama, T., Ishihara, S., Tang, H., Amasaki, E.R.Y., Akai, S., Okoyama,
511 T.E.Y., Shihara, S.H.I., Ang, H.O.T., 2013. Tin isotope analysis of cassiterites from Southeastern
512 and Eastern Asia. *Geochem. J.* 47, 21–35.

513 Yang, M., Liu, G., Sun, R., Chou, C.L., Zheng, L., 2012. Characterization of intrusive rocks and REE
514 geochemistry of coals from the Zhuji Coal Mine, Huainan Coalfield, Anhui, China. *Int. J. Coal*
515 *Geol.* 94, 283–295. <https://doi.org/10.1016/j.coal.2011.06.012>

516 Yao, J., Mathur, R., Powell, W., Lehmann, B., Tornos, F., Wilson, M., Ruiz, J., 2018. Sn-isotope
517 fractionation as a record of hydrothermal redox reactions. *Am. Mineral.* 103, 1591–1598.

518 Yi, W., Halliday, A.N., Lee, D.C., Christensen, J.N., 1995. Indium and tin in basalts, sulfides, and the
519 mantle. *Geochim. Cosmochim. Acta* 59, 5081–5090.
520 [https://doi.org/10.1016/0016-7037\(95\)00342-8](https://doi.org/10.1016/0016-7037(95)00342-8)

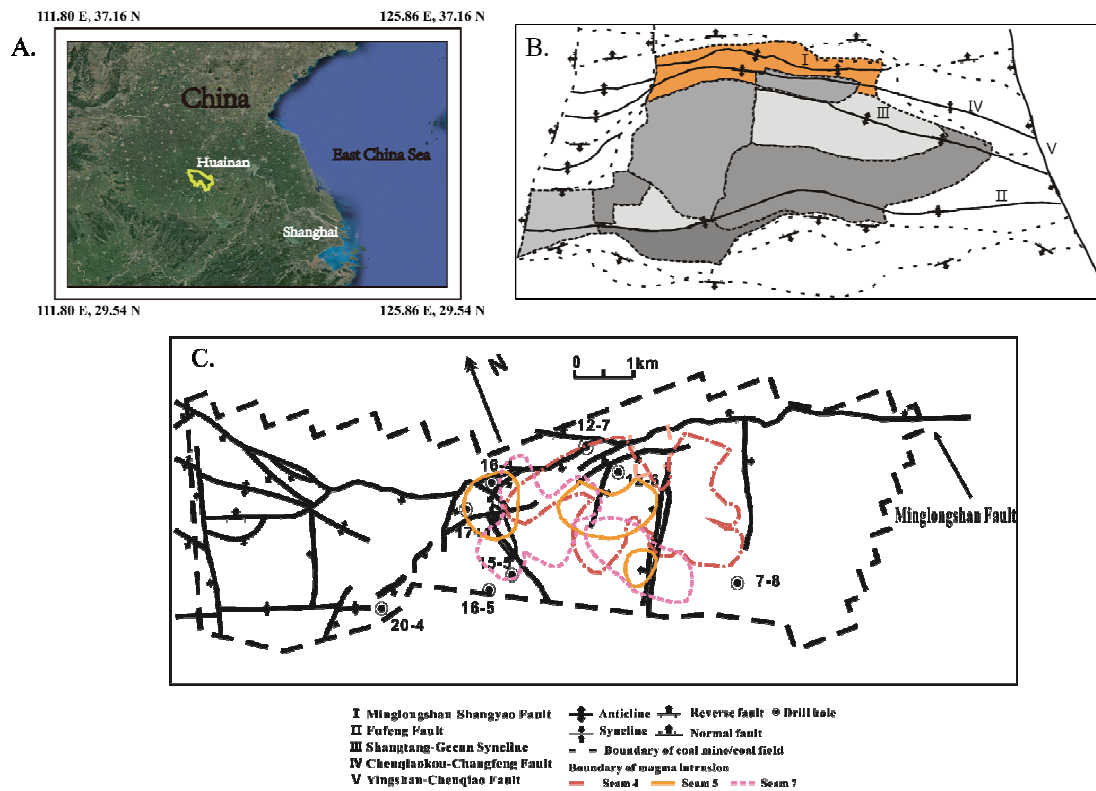


Fig. 1 A) Location of Huainan Coalfield, B) Main faults in Huainan Coalfield, and C) Locations of minor faults and sample drilling holes, and magma intrusion boundaries of coal seam No.4, No.5 and No.7 in Zhuji Coal Mine, Huainan Coalfield

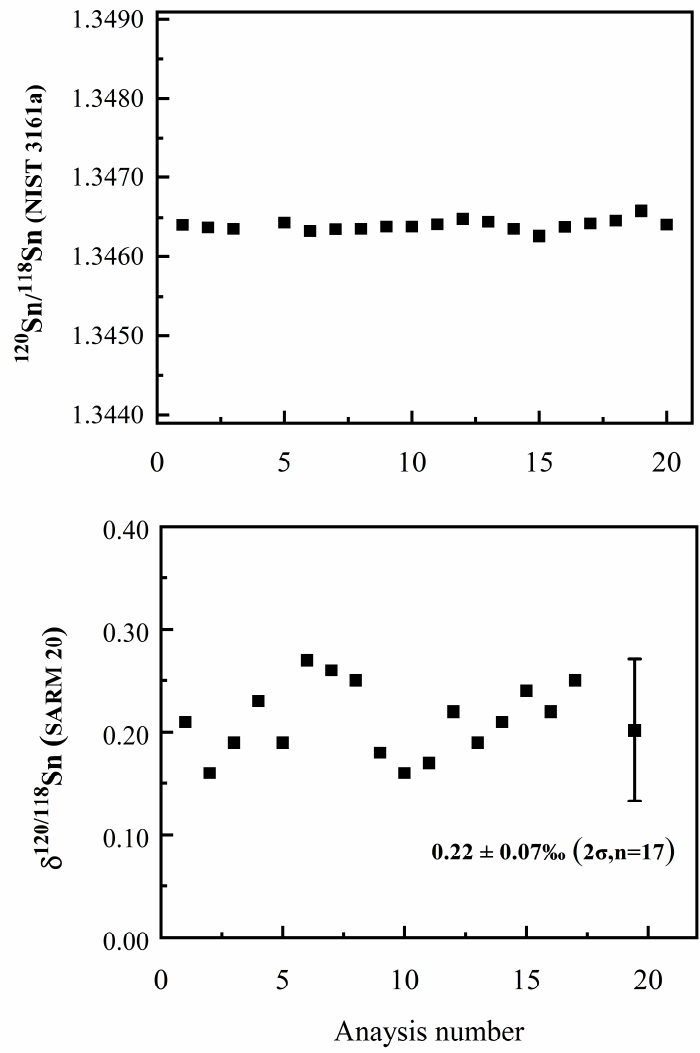


Fig. 2 Analytical precision of standard solution of NIST 3161a and coal standard SARM 20

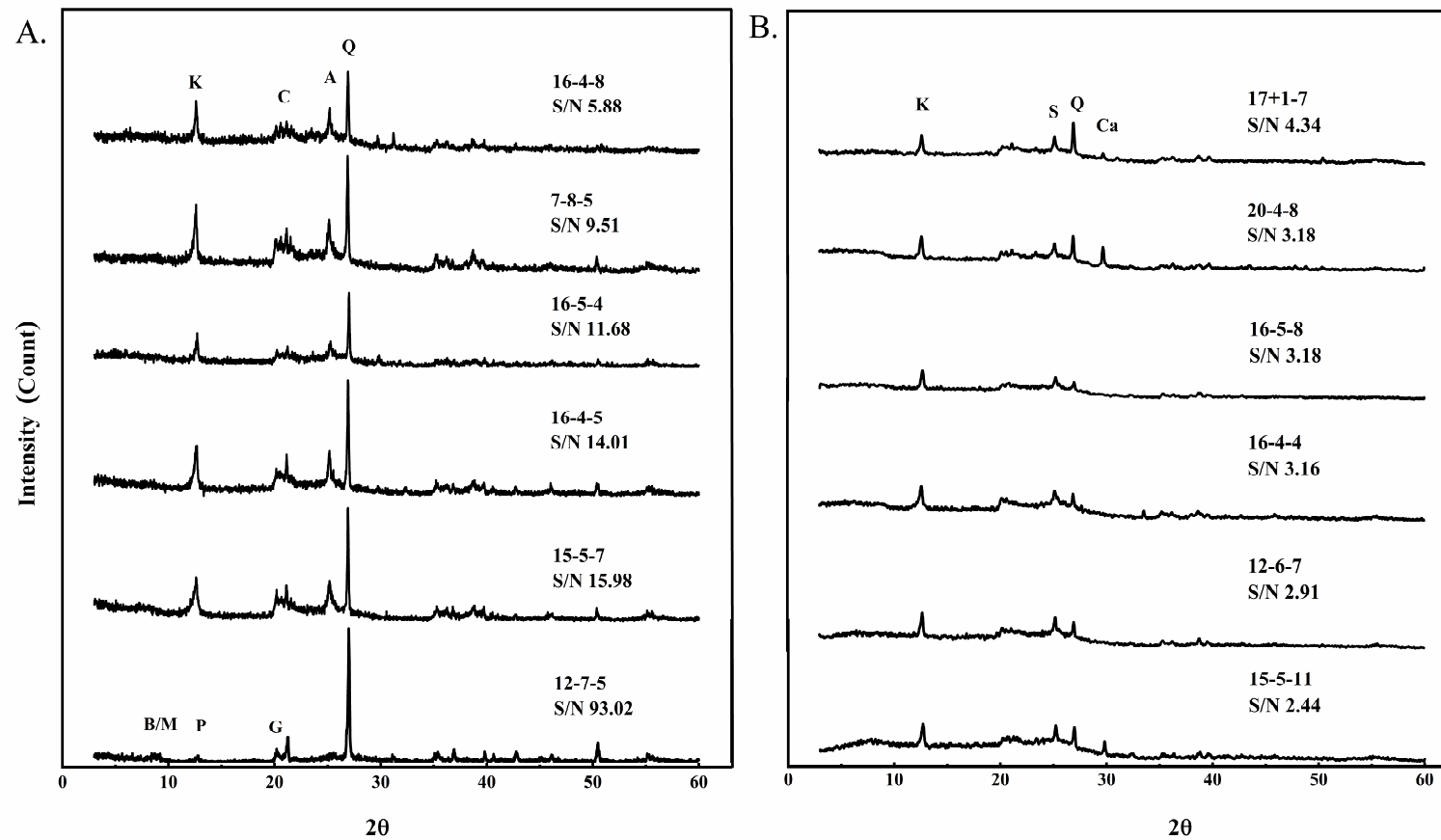


Fig. 3 XRD spectras of the coal samples. The intensities of the samples were normalized basing on sample #12-7-5. The samples were classified into two groups by their calculated S/N. A) Group Min, B) Group Org.

K: Kaolinite, Q: Quartz, M: Muscovite, B: Biotite, G: Gottardiite, A: Amesite, P: Preswerkite, C: Chamosite, S: Iron Sulfide, Ca: Calcite

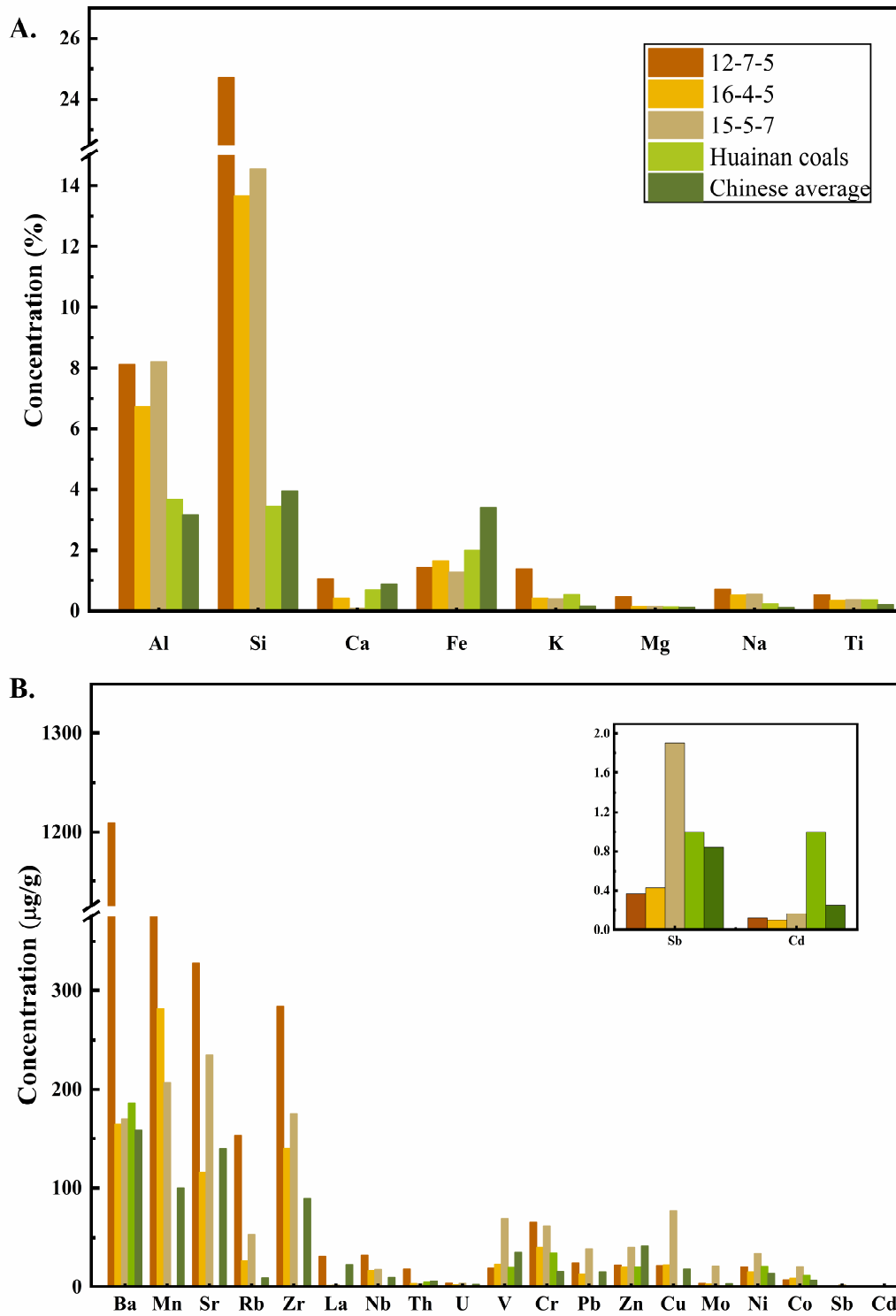


Fig. 4 Major elements levels A) and trace elements levels B) of the coals relative to Huainan coals and Chinese coal average

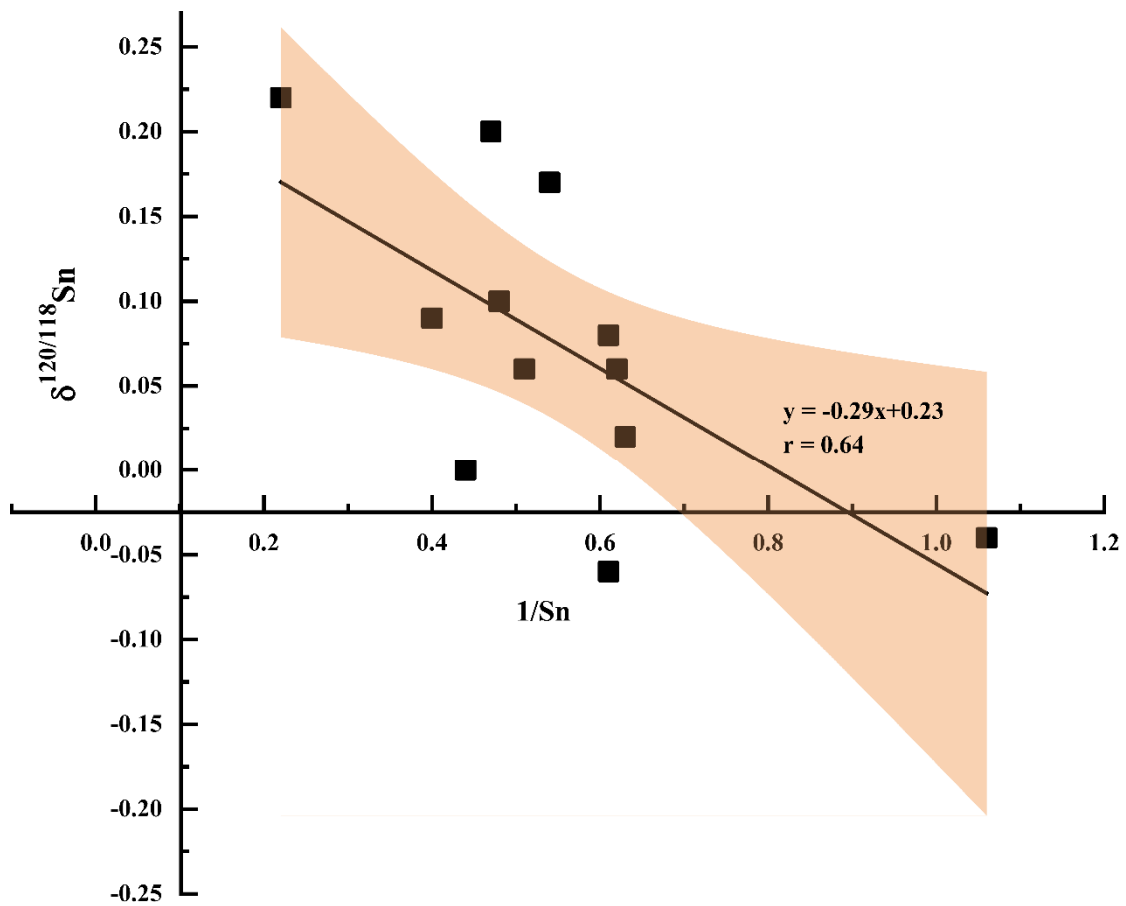


Fig. 5 Linear regression between 1/Sn concentration ($\text{g } \mu\text{g}^{-1}$) and $\delta^{120/118}\text{Sn}$ suggesting a mixing of two endmembers, the dashed zone were range of data within 95% confidential intervals

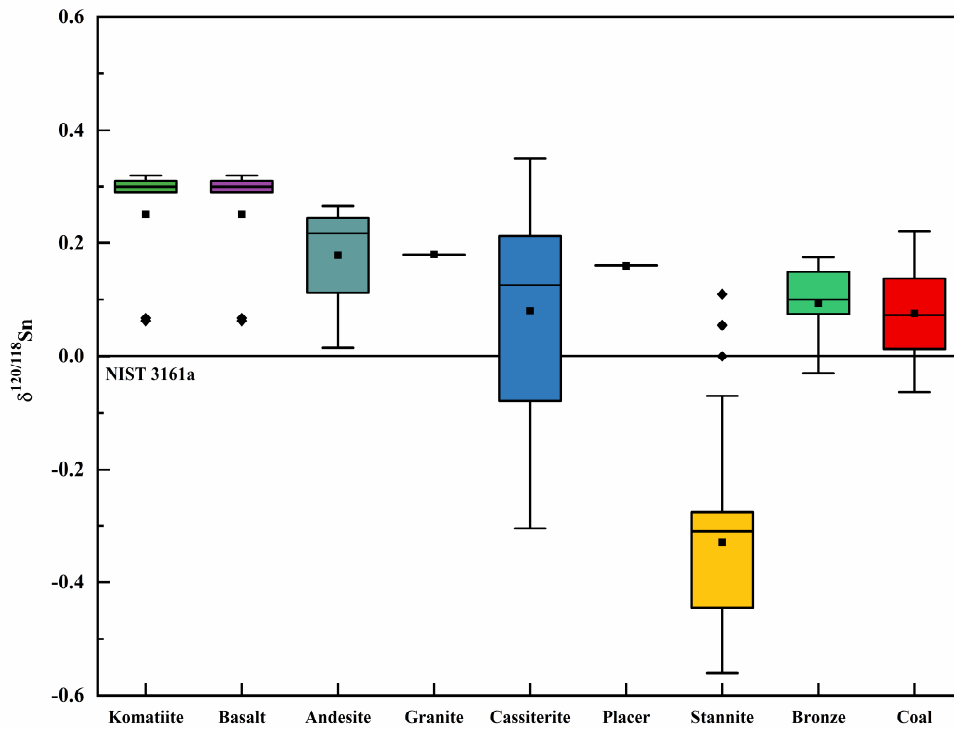


Fig. 6 A combination of $\delta^{120/118}\text{Sn}$ values in terrestrial samples. Data of $\delta^{120/118}\text{Sn}$ in coals are from this study. Other data are from Wang D. et al. (2019), Yao et al.(2018), Creech et al. (2017), Badullovich et al. (2017), Wang et al. (2018 and 2017), Yamazaki et al. (2014 and 2013). The black rectangle refers the median and the black diamond refers the outlier. For comparison purposes, all the Sn isotope ratios were converted to $\delta^{120/118}\text{Sn}$ relative to NIST 3161a. Tin isotope differences between reference solutions used in the literatures and NIST 3161a were corrected using the values measured by She et al. (2019).

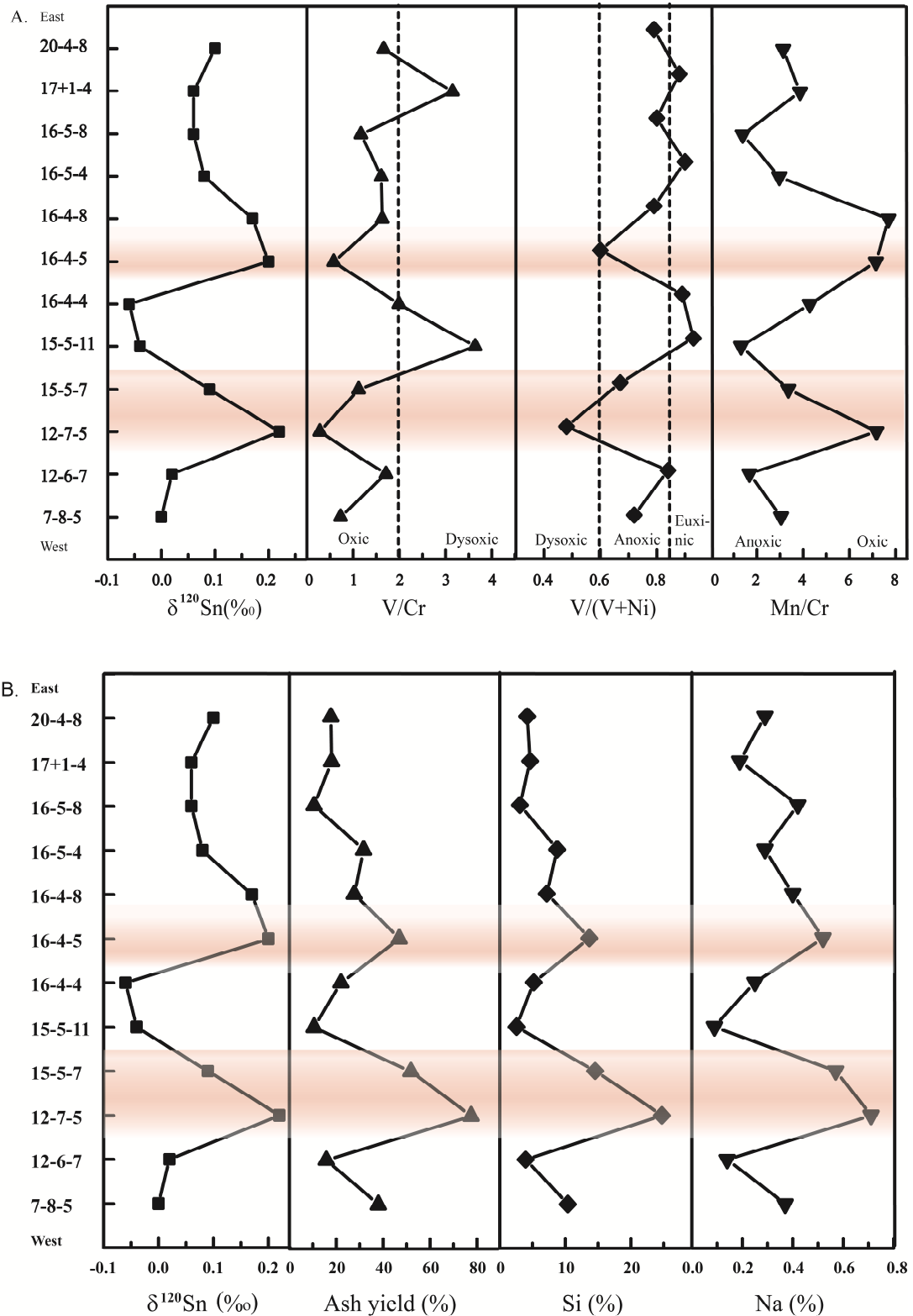


Fig. 7 A) The spatial distribution of $\delta^{120/118}\text{Sn}$, V/Cr, V/(V+Ni) and Mn/Cr. The sample order on the vertical axis represents the locations of the drill holes from west to east. The shadowed rectangle highlights the samples which were probably affected by magmatic hydrothermal solution. The empirical thresholds of V/Cr and V/(V+Ni) for redox states were from Hatch and Leventhal (1992), Nico et al. (2009) and Rimmer (2004). Mn/Cr only qualitatively indicates redox state changes as Mn

and Cr behave inversely in terms of solubility under oxic and reduced conditions (Jones and Manning, 1994; Rimmer, 2004). B) The spatial distribution of $\delta^{120/118}\text{Sn}$, ash content, Si and Na concentrations.

Table 1 Sample information

Sample ^a	Coal seam	Depth (m)	Degree of the coalification ^b	A _d (%)	Total Sn in sample (µg/g)	$\delta^{120/118}\text{Sn}$ (‰)	2SD
12-7-5	Seam 5	1182.6	Natural Coke	78.53	4.48	0.22	0.07
16-4-5	Seam 5	1107.42-1106.77	Bituminous	46.85	2.12	0.20	0.07
16-4-8	Seam 8	1041.42-1038.78	Bituminous	27.66	1.85	0.17	0.07
16-4-4	Seam 4	1121.40-1116.92	Bituminous	21.99	1.65	-0.06	0.07
7-8-5	Seam 5	1105.82-1104.52	Bituminous	37.95	2.28	0.00	0.07
12-6-7	Seam 7	1018.40-1017.15	Bituminous	15.79	1.60	0.02	0.07
15-5-7	Seam 7	1080.7-1079.98	Natural Coke	51.87	2.49	0.09	0.07
15-5-11	Seam 11	987.75	Sub-bituminous	10.53	0.94	-0.04	0.07
16-5-4	Seam 4	1125.22-1122.92	Bituminous	31.63	1.63	0.08	0.07
16-5-8	Seam 8	1050.50-1046.90	Bituminous	17.99	1.95	0.06	0.07
20-4-8	Seam 8	1064.10	Bituminous	17.68	2.09	0.10	0.07
17+1-4	Seam 4	1121.25-1117.80	Bituminous	10.53	1.61	0.06	0.07

a. These samples were firstly reported in the study of Sun et al. (2010)

Table 2 Procedures for Sn separation from coal matrix (modified from Wombacher et al., 2003; Yi et al., 1995)

Operation	Solvents
First step	2mL AG 1-X8 (resin loading)
Washing	10mL 2M HNO ₃ , then 2mL Milli-Q
Conditioning	10mL 3M HCl
Loading	5mL 3M HCl (sample Sn in presence of 100 µL 3M HF)
Matrix Elution 1	35mL 0.5M HCl
Matrix Elution 2	10mL 1M HCl
Matrix Elution 3	10mL 2M HCl
Matrix Elution 4	12mL 8M HCl
Sn Collection	12mL 2M HNO ₃ Add 100 µL 3M HF to recipient
Washing	10mL 4M HNO ₃
Second step	2mL TRU resin
Washing	10mL 0.5M HNO ₃ , 10mL Milli-Q 2 cycles
Conditioning	10mL 0.5M HCl
Loading	8mL 0.5M HCl (add 100 µL 3M HF)
Matrix Elution 1	16mL 0.5M HCl
Trace Elution 2	10mL 0.25M HCl
Sn Collection	10mL Milli-Q (Add 100µL 3M HF to recipient)
Sn Collection	5mL 0.4M HNO ₃
Washing	10 mL 0.5M HNO ₃ , 10mL Milli-Q